PHYSICAL REVIEW B **84**, 165328 (2011)

Effective mass modeling of excitons in type-II quantum dot heterostructures

E. J. Tyrrell and J. M. Smith
Department of Materials, University of Oxford, Parks Road, Oxford OX1 3PH, United Kingdom

(Received 19 May 2011; revised manuscript received 10 August 2011; published 27 October 2011)

We present a study of CdTe/CdSe and CdSe/CdTe type-II core-shell nanocrystals using a (2,6)-band effective mass approximation for quantum-dot heterostructures and map the exciton properties as a function of core radius and shell thickness. The Coulomb interaction (including the effects of dielectric mismatch) is calculated in first-order perturbation theory, and optical absorption wavelengths of the two structures are compared. We find that the (2,6)-band theory allows us to identify higher exciton states in absorption data for CdTe/CdSe which a single-band theory does not, thereby demonstrating the importance of an accurate description of the nanocrystal valence band structure. Excitation probabilities are significantly lower and the number of allowed transitions greater in the (2,6)-band theory due to *s*-*d* mixing in the hole wave functions.

DOI: 10.1103/PhysRevB.84.165328 PACS number(s): 73.22.−f, 78.67.Bf, 81.07.−b

I. INTRODUCTION

Modern colloidal chemistry allows fabrication of semiconductor nanocrystals (NCs) with different shapes and compositions; the combination of more than one semiconductor in a NC produces a heterostructure, or hetero-NC. Such multicomponent nanostructures provide the opportunity of tuning material properties via wave function engineering. Various types of heterostructure nanocrystal have been synthesized, including core-shell NCs,[1,2] three-layer quantum-dot quantum wells,[3,4] and shape-controlled nanoparticles such as heteronanorods[5] and tetrapods.[6] The energetic alignment of the bulk conduction and valence band edges of the constituent materials at a heterointerface determines how the carriers are localized, and choice of these band alignments can have a profound effect on the physical properties of the nanocrystal. In type-I structures, the band edges of one semiconductor are located within the energy gap of the other semiconductor so that both electron and hole localize in the narrower-gap material. Type-II heterostructure NCs, in which the conduction and valence bands have a staggered alignment, offer an alternative design in which the lowest-energy states for conduction band electrons and valence band holes lie in different spatial regions, leading to charge separation between the carriers. Type-II NCs can be classified[7] according to whether their band alignments tend to localize the hole in the core and the electron in the shell [*h*/*e* structures, Fig. 1(a)] or the electron in the core and the hole in the shell [*e*/*h* structures, Fig. 1(b)]. The spatial separation of the carriers has a number of useful physical consequences. It allows NC band gaps of lower energy than the band gap of either constituent semiconductor;[7] it can also allow tuning of carrier-carrier interactions that may lead to applications in nonlinear optics,[8,9] lasing,[10] and photovoltaic cells.[11,12] For lasing applications, it has been shown that Auger recombination can be controlled and suppressed,[13] leading to longer optical gain lifetimes. In addition, it has been shown that by reversing the sign of the exciton-exciton interaction energy in type-II NCs optical gain in the single-exciton regime is possible.[14] The starting point in the design of type-II heterostructure nanocrystals for many applications must be a detailed understanding of single-exciton states, which determine many of the important optical properties and provide a basis for understanding more complex situations such as multiple excitons. The behavior of parameters such as the carrier self-energies and interparticle Coulomb energies is considerably richer than that of type-I core-shell NCs, so it is worthwhile to develop a comprehensive picture of how they vary as functions of the core and shell dimensions. Others have used the effective mass approximation (EMA) for quantum-confined carriers to model the emission spectra,[15] electron-hole overlap,[14] and biexciton energies[7]of type-II NCs, but calculations presented to date often assume single energy bands for the electron and hole (which we refer to as single-band models) and infinite confining potentials, thereby considerably simplifying the calculation of single-particle states and their Coulomb interaction. In this paper we extend the calculations to higher hole levels using both a single-band and a (2,6)-band approach to assess the effect of the valence band structure, and include the effects of a finite confining potential on the wave functions. The (2,6)-band approach uses the 2×2 electron and 6×6 hole Hamiltonians developed by Pokatilov *et al.*[16] for quantum-dot heterostructures, which take into account correct operator ordering at the heterointerfaces,[16] the complex valence band structure, and coupling between valence and conduction bands.[17] These Hamiltonians are valid over the entire heterostructure,[16] in contrast to earlier multiband calculations,[18–20] which used Hamiltonians derived assuming homogeneous material parameters (application of these to heterostructures may lead to nonunique matching of the homogeneous solutions at material boundaries[16]). We compare single-particle states calculated in the single-band and (2,6)-band models and include the Coulomb interaction as a first-order perturbation to calculate exciton energies. We show that the (2,6)-band theory enables the identification of four higher exciton transitions in experimental data for CdTe/CdSe NCs, which the single-band theory does not, and the absence of *s*-*d* mixing in the single-band theory leads it to underestimate the number of allowed transitions.

II. EFFECTIVE MASS MODELS

The conduction and valence band profiles of the core-shell NCs are modeled using bulk material parameters, with a finite band gap E_{g3} in the surrounding material and equal potential barriers for the electron and hole (Fig. 1). We

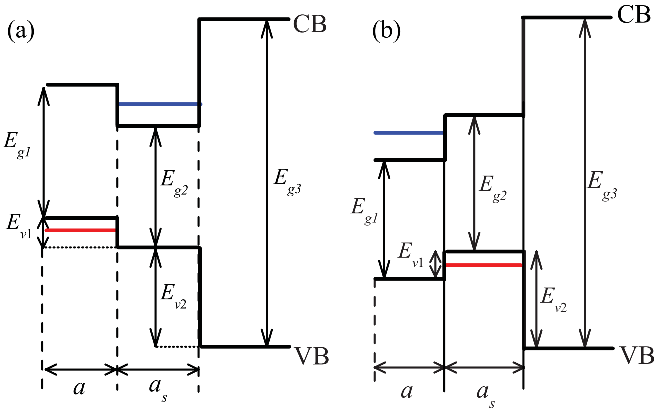

FIG. 1. (Color online) Type-II band alignments in (a) *h*/*e* and (b) *e*/*h* core-shell NCs with core radius a and shell thickness a_s. E_{g1}, E_{g2}, and E_{g3} represent the band gaps of the core, shell, and matrix materials, respectively. E_{v1} and E_{v2} are the valence band offsets. CB denotes the conduction band and VB the valence band. The blue and red horizontal lines indicate quantum-confined energy levels of the electron and hole, respectively, in the type-II limit of spatially separated carriers.

assume spherically symmetric NCs with core radius a and shell thickness a_s.

Different localization regimes result from different combinations of a and a_s. Energy criteria are used to classify carriers as primarily core or shell localized.[7] For the *h*/*e* NC [Fig. 1(a)] the electron is shell localized if its energy lies below the conduction band edge of the core material, i.e., $E_e < E_{g1}$ (electron energy E_e measured from the core valence band edge) and the hole core localized if $|E_h| < E_{v1}$ where E_h is the hole energy. For the *e*/*h* NC [Fig. 1(b)] the electron is considered core localized if the energy level lies below the bulk conduction band minimum of the shell semiconductor, i.e., $E_e < E_{g2}$ (E_e measured from the shell valence band edge) and the hole is considered shell localized if its level lies above the valence band offset at $-E_{v1}$, i.e., $|E_h| < E_{v1}$.

A. Single-particle calculations

1. Single-band model

Electron and hole wave functions are of the form $\Psi^{e(h)}_{lm}(\mathbf{r}) = R^{c(v)}_l(r)Y_{lm}(\theta,\phi)$, where R_l is the radial function, Y_{lm} is the spherical harmonic,[21] and the parity $p = (-1)^l$. The conduction and valence bands are described by parabolic bands whose curvature is determined by the electron and hole effective masses m_e and m_h. We apply the BenDaniel-Duke boundary conditions[22,23] at the material boundaries to calculate electron (hole) energies E_e (E_h). Electron (hole) levels are labeled nq (nQ) where $q = s,p,d,\dots$ ($Q = S,P,D,\dots$) denote the envelope angular momentum l, and n is the level number. The excitation probability P_t of the electron-hole pair state $\Psi^{e*}_{lm}\Psi^{h}_{l'm'}$ is

$$P_t = \delta_{mm'}\delta_{ll'}\left|\int R^{c*}_l R^{v}_{l'} r^2 dr\right|^2, \tag{1}$$

where $\delta_{ll'}$ represents the Kronecker delta.

2. (2,6)-band model

We use the energy-dependent two-band electron and six-band hole radial Hamiltonians derived by Pokatilov *et al.*[16] for quantum-dot heterostructures to calculate electron and hole states for spherical core-shell NCs within Burt's envelope function representation.[24–26] The Hamiltonians take into account the complex structure of the valence band and include the coupling between the conduction and valence bands through energy-dependent parameters.[17] Due to spherical symmetry, the wave functions are eigenfunctions of the total angular momentum j, its z component m, and its parity p.[16] In the notation of Efros and Rosen (ER) the electron and hole wave functions are[27]

$$\Psi^{e\pm}_{j,m}(\mathbf{r}) = R^{\pm}_{c,j}\sum_{\mu=-1/2}^{1/2}\Omega^{c}_{\mu}u^{c}_{\mu}, \tag{2}$$

$$\Psi^{h\pm}_{j,m}(\mathbf{r}) = \sum_{i=1}^{2}\sum_{\mu=-3/2}^{3/2} R^{\pm}_{hi,j}\Omega^{hi}_{\mu}u^{v}_{3/2,\mu} + R^{\pm}_{s,j}\sum_{\mu=-1/2}^{1/2}\Omega^{s}_{\mu}u^{v}_{1/2,\mu}, \tag{3}$$

where $u^{c,v}_{J,J_z}$ are Bloch functions of the conduction and valence bands with band edge angular momentum J, the Ω angular functions are defined in Ref. 27, and the $\pm$ superscript denotes $p = \pm 1$. In the notation of Pokatilov *et al.* the electron and hole radial functions are[16]

$$R^{(p)}_{e,j} = R^{c;j}_{1/2,j-p/2}, R^{(p)}_{h,j} = \begin{pmatrix} R^{v;j}_{3/2,j+p/2} \\ R^{v;j}_{3/2,j-3p/2} \\ R^{v;j}_{1/2,j+p/2} \end{pmatrix} \tag{4}$$

and are related to the ER radial wave functions by[16]

$$\begin{aligned} R^{c;j}_{1/2,j-1/2} &= R^{+}_{c,j}, & R^{c;j}_{1/2,j+1/2} &= -R^{-}_{c,j}, \\ R^{v;j}_{3/2,j+1/2} &= R^{+}_{h1,j}, & R^{v;j}_{3/2,j-1/2} &= R^{-}_{h1,j}, \\ R^{v;j}_{3/2,j-3/2} &= -R^{+}_{h2,j}, & R^{v;j}_{3/2,j+3/2} &= -R^{-}_{h2,j}, \\ R^{v;j}_{1/2,j+1/2} &= R^{+}_{s,j}, & R^{v;j}_{1/2,j-1/2} &= R^{-}_{s,j}. \end{aligned} \tag{5}$$

Independent electron (hole) energies E_e (E_h) are then calculated by imposing continuity of the electron (hole) radial wave functions $R^{(p)}_{e(h),j}$ and the radial probability current[16] at the material boundaries at $r = a$ and $r = a + a_s$. For example, at $r = a$

$$\left(R^{(p)}_{e(h),j}\right)_A\big|_{r=a-} = \left(R^{(p)}_{e(h),j}\right)_B\big|_{r=a+}, \tag{6}$$

$$\hat{\mathcal{J}}^{(p)}_{e(h),j}\left(R^{(p)}_{e(h),j}\right)_A\big|_{r=a-} = \hat{\mathcal{J}}^{(p)}_{e(h),j}\left(R^{(p)}_{e(h),j}\right)_B\big|_{r=a+}, \tag{7}$$

with similar equations for $r = a + a_s$. $\hat{\mathcal{J}}^{(p)}_{e(h),j}$ is the radial component of the electron (hole) current operator and A and B denote the core and shell regions, respectively. The resulting equations are solved numerically. Energies are measured from the top of the core valence band for the *h*/*e* NC and from the top of the shell valence band for the *e*/*h* NC. Electron (hole) states are labeled nq_j (nQ_j), where $q = s,p,d,\dots$ ($Q = S,P,D,\dots$) denotes the lowest value of the envelope angular momentum l in the overall wave function and n is the level number. $Q = j - p/2$ for electrons and $Q = \min(j + p/2, |j - 3p/2|)$ for holes.[16] Momentum matrix elements are calculated for electron-hole pairs $1s_{1/2}nS_{3/2}$ $(n = 1,2,3)$ to measure the change in strength of optical transitions as a function of a and a_s. We define the excitation probability $P_{m,m'}$ of the pair state $\Psi^{e\pm *}_{j,m}\Psi^{h\pm}_{j',m'}$ to be proportional to the square of the momentum matrix element:[28,29]

$$P_{m,m'} = \left| \int \delta(\mathbf{r}_e - \mathbf{r}_h)\Psi^{e\pm *}_{j,m}(\mathbf{r}_e)\frac{\mathbf{e}\cdot\mathbf{p}}{P(\mathbf{r})}\Psi^{h\pm}_{j',m'}(\mathbf{r}_h)d\mathbf{r}_e d\mathbf{r}_h \right|^2, \tag{8}$$

where $\mathbf{p}$ is the momentum operator, $\mathbf{e}$ is the polarization of incident light, and $P = \langle S|\hat{p}_z|Z\rangle$ is the Kane momentum matrix element. For the NCs studied here, $P(r)$ factors out because $P_{\mathrm{CdTe}} \approx P_{\mathrm{CdSe}}$ (see Sec. III A 1).

B. Coulomb interation

We work in the strong-confinement limit so the exciton wave function Ψ_{exc} is approximated by the wave function of the electron-hole pair: $\Psi_{\mathrm{exc}} = \Psi^{e*}\Psi^h$, where Ψ^e (Ψ^h) is the electron (hole) wave function in either EMA model. First-order perturbation theory gives the exciton energy as

$$E_{\mathrm{exc}} = E_e - E_h + \langle \Psi^h | \langle \Psi^e | U | \Psi^e \rangle | \Psi^h \rangle \tag{9}$$

where U is the Coulomb energy for the electron-hole pair, which for a system with a spatially varying dielectric constant $\varepsilon(r)$ is[30]

$$U(\mathbf{r}_e,\mathbf{r}_h) = V_c(\mathbf{r}_e,\mathbf{r}_h) + V_s(\mathbf{r}_e) + V_s(\mathbf{r}_h), \tag{10}$$

where V_c is the interparticle Coulomb potential and V_s is the self-polarization potential. The potential $V_c = V_d + V_p$, where V_d is the "direct" interparticle Coulomb potential [Fig. 2(a)] and V_p is the interface polarization potential[7] [Fig. 2(b)] due to the interaction between a particle and the induced charge of the other particle. The self-polarization potential V_s arises from the interaction of a particle and its own induced charge[31] [Fig. 2(c)]. We calculate V_c and V_s by applying the numerical method of Bolcatto and Proetto[31] to core-shell NCs by assuming a smooth spherically symmetric dielectric profile $\varepsilon(\mathbf{r}) = \varepsilon(r)$ which changes over distances of $2\delta_1$ and $2\delta_2$ at the inner and outer material boundaries, respectively [Fig. 2(c), inset]. This is modeled by discretizing the region $a - \delta_1 < r < a + a_s + \delta_2$ into $N - 1$ slices where $N = 500$. This is expected to describe the actual NC dielectric profile more realistically than the commonly used "steplike" profiles that assume an abrupt change of constant at the material boundaries and localize all self-induced charge there, causing discontinuities in the self-polarization potential. In particular, this method avoids the infinite discontinuity at $r = a + a_s$ in such models, which is incompatible with the use of a finite potential well in the surrounding medium. The self-polarization potential is[31]

$$V_s^m(r) = \frac{e^2}{8\pi\varepsilon_0\epsilon_m}\sum_{l=0}^{\infty}\frac{1}{1 - p_{m,l}q_{m,l}} \times (p_{m,l}r^{2l} + p_{m,l}q_{m,l}r^{-1} + q_{m,l}r^{-2(l+1)}), \tag{11}$$

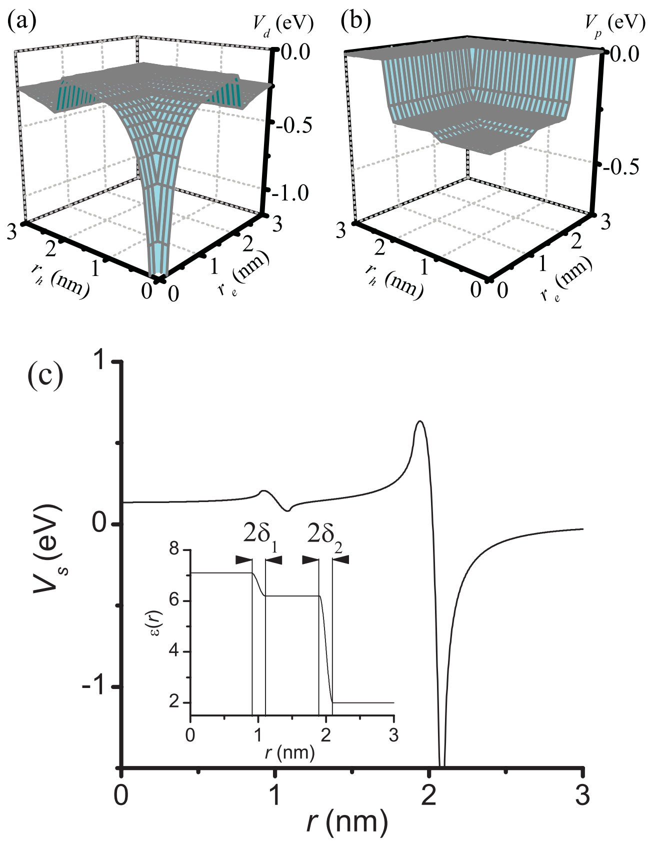

FIG. 2. (Color online) The $l = 0$ component of (a) the direct Coulomb potential V_d and (b) the interface polarization potential V_p with (c) the self polarization potential V_s corresponding to the dielectric profile shown in the inset for a CdTe/CdSe NC with $a =$ 1 nm, $a_s = 1$ nm and $\delta_1 = \delta_2 = 0.1$ nm.

and the $l = 0$ component of the interparticle Coulomb potential is[31,32]

$$V_{c,0}(\mathbf{r_e},\mathbf{r_h}) = \begin{cases} \dfrac{-e^2}{4\pi\varepsilon_0\epsilon_m}(p_{m,0} + r_>^{-1}), & \text{if } i \leqslant m \\ \dfrac{-e^2}{4\pi\varepsilon_0\epsilon_m}(p_{i,0} + r_>^{-1})\displaystyle\prod_{j=m+1}^{i}\frac{1 + p_{j-1,0}R_{j-1}}{1 + p_{j,0}R_{j-1}}, & \text{if } i > m \end{cases} \tag{12}$$

The $p_{m,l}$ and $q_{m,l}$ are recursive coefficients (see Ref. 31 for full definitions). In Eq. (12) the index i (m) indicates that the particle with coordinate $\mathbf{r}_e$ $(\mathbf{r}_h)$ is located in the ith (mth) slice of the discretized region, and R_i is the radial coordinate of the ith slice. ϵ_m is the dielectric constant in the mth slice. V_d is given by the terms proportional to $1/r_> = 1/\max(r_e,r_h)$, and V_p is given by those proportional to $p_{i,j}$. We find that $V_p = 0$ for $r > a + a_s + \delta_2$ since there is no induced charge outside the NC outer dielectric interface, and V_d corresponds to the classical interparticle Coulomb interaction. V_d is unaffected by the external dielectric constant ε_3 while V_p increases in magnitude as the dielectric mismatch increases.

The interparticle Coulomb energy E_c and self-polarization energies $E_{s,i}$ $(i = e,h)$ are

$$E_c = \langle\Psi^h|\langle\Psi^e|V_c(\mathbf{r}_e,\mathbf{r}_h)|\Psi^e\rangle|\Psi^h\rangle, \quad (13)$$

$$E_{s,i} = \langle\Psi^h|\langle\Psi^e|V_s(\mathbf{r}_i)|\Psi^e\rangle|\Psi^h\rangle. \quad (14)$$

Figure 2(c) (inset) shows the profile used for a CdTe/CdSe NC. We assume $\delta_1 = \delta_2 = 0.1$ nm for both NCs so the interface regions are of the order of a lattice constant in width. For the NC we use high-frequency dielectric constants, $\varepsilon_{\mathrm{CdTe}} = 7.1$ (Ref. 33), $\varepsilon_{\mathrm{CdSe}} = 6.2$ (Ref. 34), and $\varepsilon_3 = 2$ for $r > a + a_s + \delta_2$.

Following Eqs. (9) and (10) the exciton energies are

$$E_{\mathrm{exc}} = E_e - E_h + E_c + E_{s,e} + E_{s,h}. \quad (15)$$

III. NUMERICAL RESULTS AND DISCUSSION

A. Single-particle calculations

1. Single-particle energies

The effective mass parameters used to model the nanocrystals are shown in Table I. We assume that the CdTe/CdSe and CdSe/CdTe NCs have zinc-blende crystal structures, in accordance with structural characterization measurements.[35,43] $E_p = 2P^2/m_0$ is the Kane energy and Δ is the spin-orbit splitting. Modified Luttinger parameters γ and γ_1 were calculated in the spherical approximation using $\gamma_1^L = 5.37$, $\gamma_2^L = 1.67$, and $\gamma_3^L = 1.98$ for CdTe,[27] and $\gamma_1^L = 3.33$, $\gamma_2^L = 1.11$, and $\gamma_3^L = 1.45$ for CdSe.[36] We use a valence band offset of 0.4 eV for the CdTe/CdSe heterointerface to give the best fit to the absorption data of Oron *et al.*[37]

For the external medium we assume single-band parabolic dispersion relations for the carriers, following Ref. 38 by setting $\gamma_1 = 1, \gamma = 0, \alpha = 1$, and $E_p = 0$. We set $E_{g3} = 8$ eV to represent the organic ligands and external medium. In Fig. 3 we compare the bulk band structure of the two NC materials arising from the two models calculated using the parameters in Table I. It is seen that the (2,6)-band theory electron dispersions (solid lines) of both materials deviate from the parabolic model (dashed lines) for higher energies due to coupling with the valence band, which tends to reduce their energy. We also see that in CdTe, the parabolic model follows the heavy-hole (hh) and light-hole (lh) bands reasonably well, lying between the two for energies up to ≈1.5 eV. However, in CdSe the proximity of the spin-orbit split-off (so) band means that the parabolic (single-band) dispersion diverges significantly from the lh and hh dispersions. Since we expect optical transitions between the conduction and valence bands to involve mainly the $J = 3/2$ subbands, this deviation will have a large effect on the predicted transition energies in the single-band model compared to the (2,6)-band model.

TABLE I. Effective mass parameters used to model CdTe/CdSe and CdSe/CdTe NCs.

	CdTe	CdSe	Matrix
E_g (eV)	1.56[a]	1.75[a]	8
E_p (eV)	17.9[b]	17.5[a]	0
Δ (eV)	0.953[b]	0.42[c]	0
γ	−0.056	−0.353	0
γ_1	1.545	−0.0033	1
α	0.965	−1.02	1
m_e (m_0)	0.096[b]	0.12[d]	1
m_h (m_0)	0.4[e]	0.45[f]	1

[a] Reference 39.
[b] Reference 27.
[c] Reference 40.
[d] Reference 36.
[e] Reference 41.
[f] Reference 42.

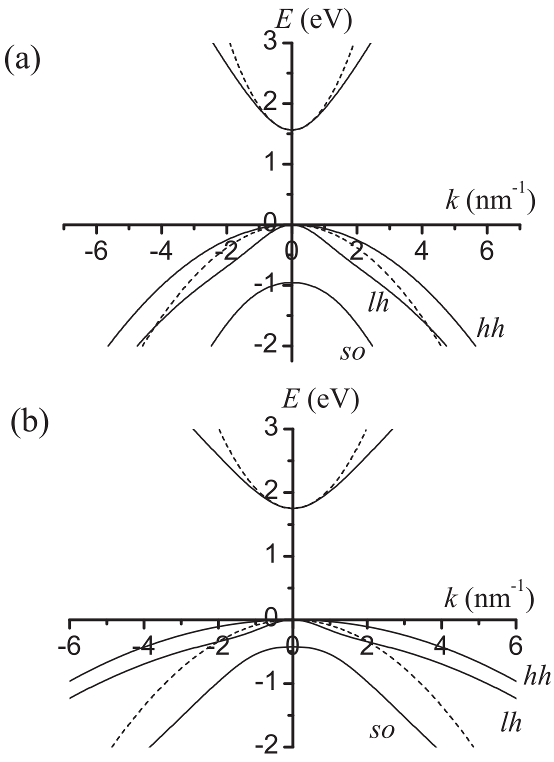

FIG. 3. Bulk band structure of (a) CdTe and (b) CdSe calculated in the (2,6)-band theory (solid lines) and single-band theory (dashed lines) using the parameters of Table I. lh, hh, and so label the light-hole, heavy-hole, and spin-orbit split-off bands, respectively.

Figure 4 shows electron and hole energies for the two NCs calculated in the single- and (2,6)-band models with localization boundaries calculated from the appropriate energy criteria. The first row shows the energy of the lowest spherically symmetric electron state, which is 1s (1$s_{1/2}$) in the single-band [(2,6)-band] model. The remaining rows show hole energies of the first three levels with S and $S_{3/2}$ symmetry in the single-band and (2,6)-band models, respectively. nS states are spherically symmetric while $nS_{3/2}$ states are not [see Eq. (2)].

The first two rows show very close agreement between the single-band and (2,6)-band electron and hole ground state energies since the band structure is approximately parabolic for low energies. The localization boundaries of CdSe/CdTe agree closely with those found in Ref. 7 for a generic e/h NC in an infinite confining potential. Black regions indicate NCs that are too small to produce confined states in the finite potential

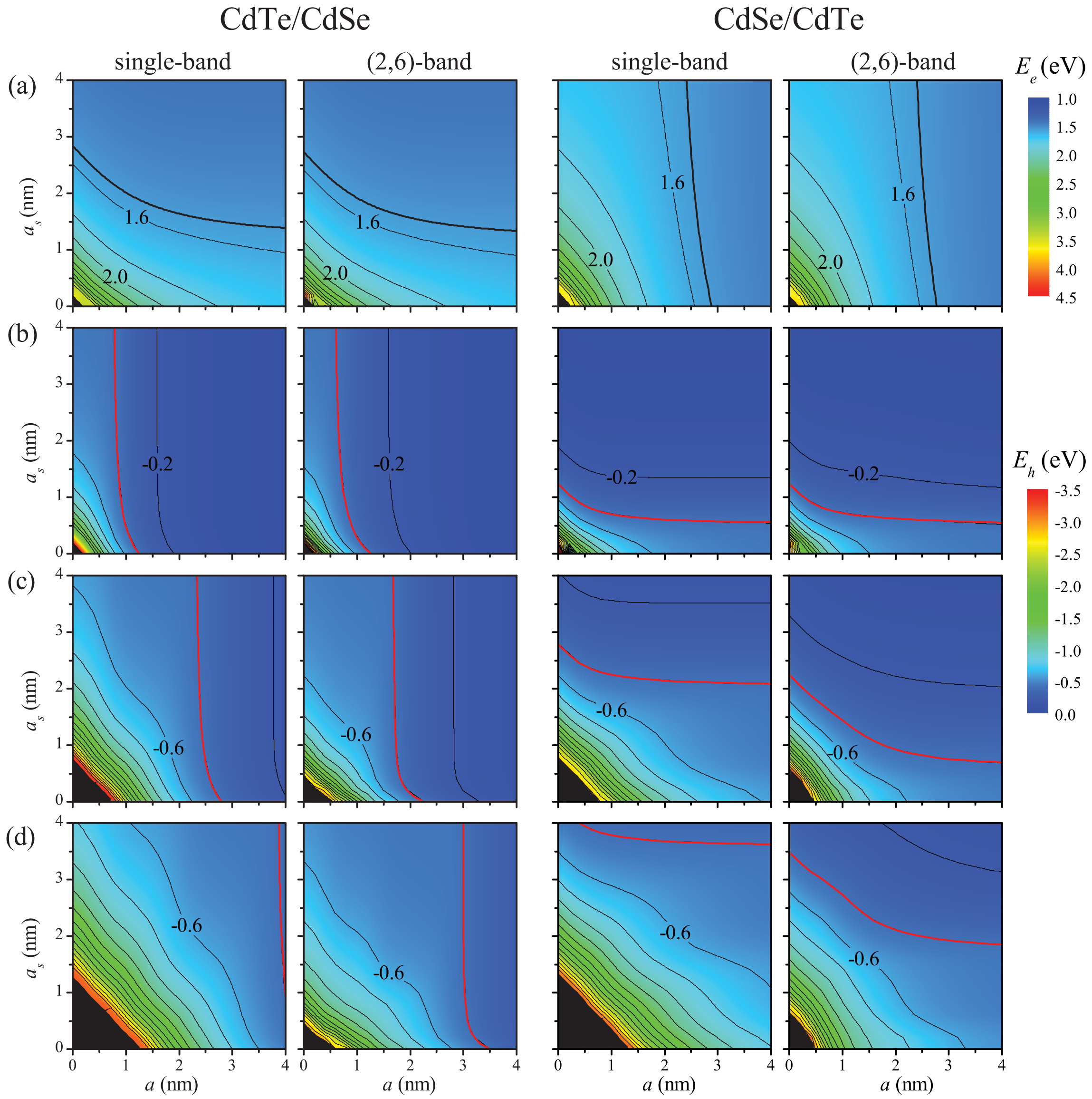

FIG. 4. (Color online) Single-particle energies in the CdTe/CdSe and CdSe/CdTe NCs calculated in the single-band model (first and third columns) and (2,6)-band model (second and fourth columns). Row (a) shows the electron ground state energy E_e for the single-band $1s$ level and the $1s_{1/2}$ (2,6)-band level. Rows (b)–(d) show the hole energy E_h for the $1S$ to $3S$ single-band levels and $1S_{3/2}$ to $3S_{3/2}$ (2,6)-band levels. Thick black and red lines denote electron and hole localization boundaries, respectively. Constant-energy contours (thin black lines) are separated by 0.2 eV intervals, wih labels in eV. Areas shaded black indicate NCs too small to produce confined states.

well. The size dependence of hole energy levels is affected by anticrossings in both models (shown by distortion of the constant-energy contours) in the direction of the confining dimension of the NC, for example looking along lines of constant a_s for the *h*/*e* NC.

In the (2,6)-band model such anticrossings affect not only the size dependence but also the character of the levels because $nS_{3/2}$ states have mixed s-d symmetry,[27] which can change due to anticrossings or interactions between levels. Generally, the amount of s-like character in the wave function decreases as the level number increases because higher angular momenta l are associated with higher energies.

Figure 4 shows that the discrepancy between hole energy levels in the two models increases with level number, as expected from the different dispersion relations in Fig. 3. We also see that the difference between the hole levels in the two theories for $n > 1$ is greater in the *e*/*h* NC than in the *h*/*e* NC. This difference in the ability of the two models to predict hole energies in the two NCs results from the deviation of the single-band dispersion from the lh and hh bands in CdSe. This is counterintuitive because the hole localizes in the shell in the CdSe/CdTe NC, but due to the valence band profile of the NC (Fig. 1), when $|E_h| < E_{v1}$, the hole is effectively confined in a finite potential well with unequal potential barriers on either side. Therefore for the second and third hole levels the corresponding radial wave functions have significant components in the core region because the potential barrier is smaller in this direction, and the band structure of the core material becomes important. Since the hole tends to localize in the core of the CdTe/CdSe NC, the valence band structure of the shell material tends to be less important for calculating confined hole levels.

2. *Excitation probabilities*

Since we work in the strong-confinement regime, the excitation probabilities of exciton states are equal to those of the corresponding electron-hole pairs. In the single-band theory the excitation probability P_t of an electron-hole pair is simply defined as an overlap integral [Eq. (1)]. In the (2,6)-band theory it is defined only between definite electron (hole) eigenstates $\Psi^{e\pm}_{j,m}$ ($\Psi^{h\pm}_{j',m'}$) with a specified polarization direction $\mathbf{e}$ [Eq. (8)]. Substituting Eqs. (2) and (3) into Eq. (8) for $1s_{1/2}nS_{3/2}$ states, we find that light with polarization $\mathbf{e}$ excites transitions between electron and hole states with the relative probabilities shown in Table II, where

$$K = \left| \int R^{+*}_{c,1/2} R^{+}_{h2,3/2} r^2 \, dr \right|^2 \tag{16}$$

and θ is the angle between $\mathbf{e}$ and the z axis. Probabilities in Table II are in agreement with those of Efros found using a four-band EMA for the holes.[29] If we then average over all polarization directions and sum over dipole-allowed transitions, we get $P_t = \frac{2}{3}K$. Equation (16) shows that because the electron is in the $1s_{1/2}$ state only the s-like components of the $nS_{3/2}$ wave functions contribute to P_t and the probability depends on the overlap of $R^{+}_{c,1/2}$ and the $l = 0$ hole envelope function $R^{+}_{h2,3/2}$. In other words, in the (2,6)-band theory only the $J = \frac{3}{2}$ valence bands contribute to the absorption or oscillator strength [see Eq. (5)] of $1s_{1/2}nS_{3/2}$ excitons despite the presence of $J = \frac{1}{2}$ components in the hole wave functions. Therefore absorption probabilities in the (2,6)-band model have a maximum value of $\frac{2}{3}$ compared to 1 in the single-band theory, where hole states are pure S states and the overlap can in theory reach unity if electron and hole densities are equal.

TABLE II. Excitation probabilities for different electron-hole pair states in the (2,6)-band theory.

m	m'	$P_{m,m'}$	m	m'	$P_{m,m'}$
$-\frac{1}{2}$	$-\frac{3}{2}$	$\frac{1}{2}K\sin^2\theta$	$\frac{1}{2}$	$-\frac{3}{2}$	0
$-\frac{1}{2}$	$-\frac{1}{2}$	$\frac{2}{3}K\cos^2\theta$	$\frac{1}{2}$	$-\frac{1}{2}$	$\frac{1}{6}K\sin^2\theta$
$-\frac{1}{2}$	$\frac{1}{2}$	$\frac{1}{6}K\sin^2\theta$	$\frac{1}{2}$	$\frac{1}{2}$	$\frac{2}{3}K\cos^2\theta$
$-\frac{1}{2}$	$\frac{3}{2}$	0	$\frac{1}{2}$	$\frac{3}{2}$	$\frac{1}{2}K\sin^2\theta$

Figure 5 shows how the excitation probability P_t changes with hole level n for the single-band $1snS$ excitons and the (2,6)-band $1s_{1/2}nS_{3/2}$ excitons.

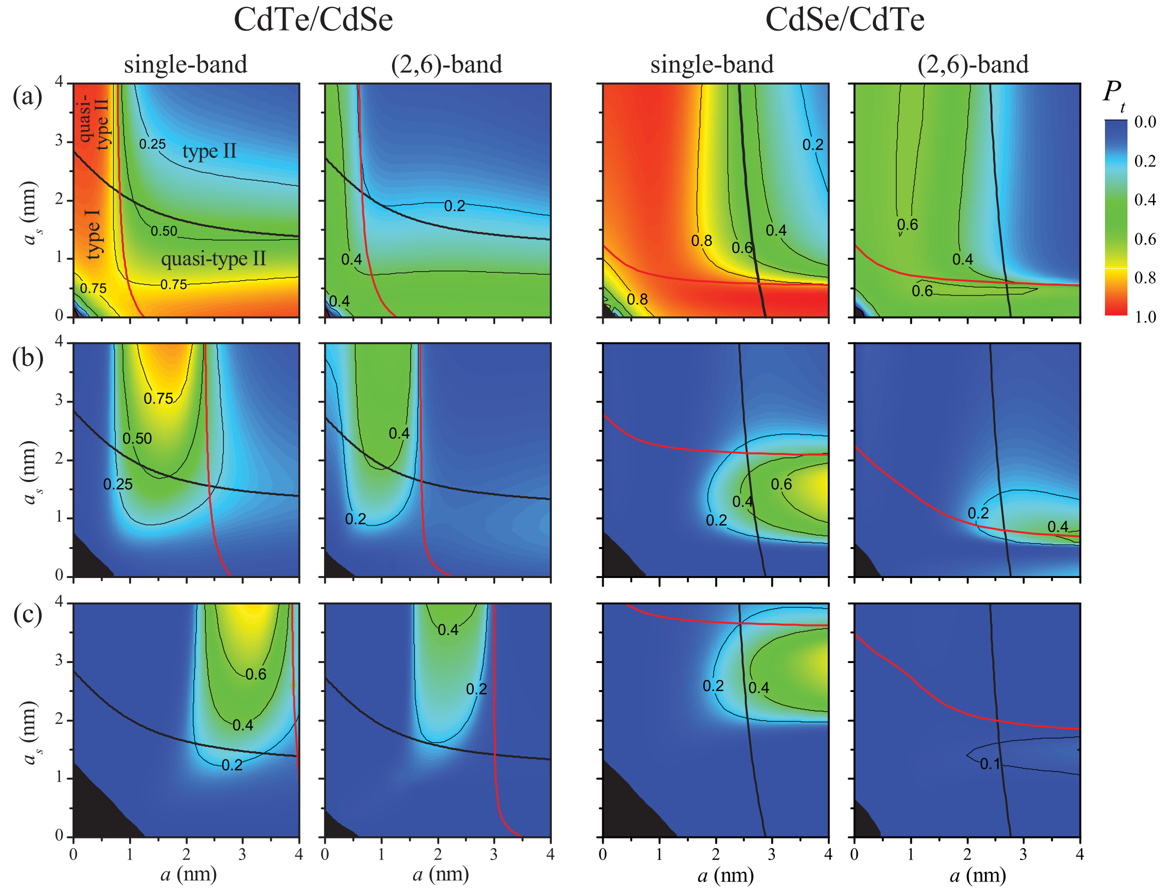

FIG. 5. (Color online) Excitation probability P_t for exciton states in the CdTe/CdSe (first two columns) and CdSe/CdTe (last two columns) NCs calculated in the single- and (2,6)-band models. Excitation probabilities for the single-band $1snS$ excitons are shown in the first and third columns and the (2,6)-band probabilities of the $1s_{1/2}nS_{3/2}$ excitons are shown in the second and fourth columns, with rows (a), (b), and (c) corresponding to $n = 1,\ 2$, and 3. Black and red lines represent electron and hole localization boundaries, respectively. Thin black lines are constant P_t contours at the values indicated.

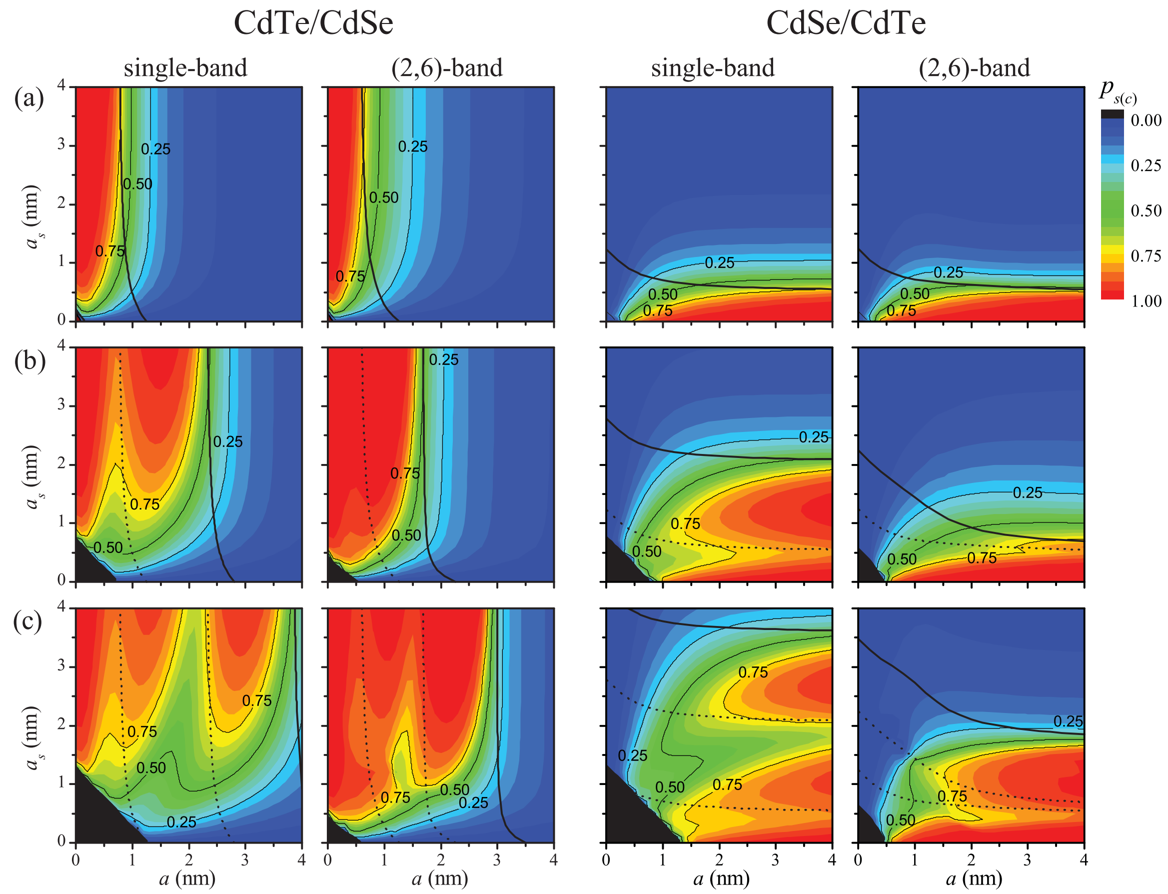

FIG. 6. (Color online) Probability $p_{s(c)}$ of finding the hole in the shell (core) region of the CdTe/CdSe (CdSe/CdTe) NC as a function of a and a_s within the two models. Single-band results for the nS levels are shown in the first and third columns while (2,6)-band results for the $nS_{3/2}$ levels are shown in the second and fourth columns; rows (a), (b), and (c) correspond to $n = 1$, 2, and 3. The hole localization boundaries of each level are shown as thick black lines and those of previous levels are shown as dotted black lines. Thin black lines are constant $p_{s(c)}$ contours at intervals of 0.25.

For the lowest exciton state in both NCs, we see that the highest probabilities occur in the type-I and quasi-type-II regimes (where wave function overlap is greatest) and the lowest in the charge-separated type-II regimes [Fig. 5(a)]. We find close agreement between our results for the $1s1S$ CdSe/CdTe exciton and those of Ref. 7.

Figure 5 shows that for $n > 1$ the areas of high P_t tend to occur in the quasi-type-II regimes, forming distinct "islands" in the (a,a_s) space that move in the direction of increasing core radius (shell thickness) for the h/e (e/h) NC. The $1s_{1/2}2S_{3/2}$ exciton of CdSe/CdTe differs slightly, having a high-probability region that lies mostly in the type-II region, where we would naively expect P_t to be low.

We can explain the origin of the high-P_t features by considering the distribution of hole probability density within the NC for these levels. We use the hole wave functions Ψ^h to calculate the probability of presence p_s (p_c) of the hole in the shell (core) region for the CdTe/CdSe (CdSe/CdTe) NCs as a function of a and a_s (Fig. 6). Figure 6 reveals that, for the lowest CdTe/CdSe hole level, most of the hole probability density is in the shell region when it is classified as delocalized (left of the localization boundary), because NCs to the left of the boundary mainly consist of the shell material ($a_s > a$). Therefore overlap of this hole density with the electron probability density in the shell gives rise to the area of high P_t in the type-I and upper left quasi-type-II regimes of Fig. 5(a). The area of high P_t in the lower right quasi-type-II regime arises from overlap between the delocalized electron and the core-localized hole.

As the CdTe/CdSe NC hole is excited we see that there are regions of high probability p_s to the left of the localization boundary of that level (thick black line), and areas of high p_s are reproduced in the plot for the next level in the same region of (a,a_s) space, leading to a series of "lobes" (colored red) that occur between the hole localization boundaries of previous levels (dotted black lines). The same sort of pattern occurs for p_c of the CdSe/CdTe NC in the direction of increasing a_s. In the (2,6)-band model, the area of high p_c between the $1S_{3/2}$ and $2S_{3/2}$ levels is very narrow due to their similar energy. The appearance of high probability lobes in approximately the same positions in (a,a_s) space as those of lower levels can be explained in terms of wave function orthogonality.[44] For a particular point in (a,a_s) space, if the radial wave function is large in the core region, the wave function of the next level in the same region will also have significant components to ensure orthogonality, leading to replication of the high-probability region. Lobes occur because the probability has to fall as the localization boundary of the current level is reached and the hole localizes in the other region of the NC.

The probability P_t is determined by the overlap of the electron and hole envelope functions. Comparing Figs. 5 and 6, we see that the overlap between the electron and hole wave functions only picks out one particular lobe of high p_s (p_c) in the *h*/*e* (*e*/*h*) NC for each level. This also originates from hole wave function orthogonality—if the overlap between the electron and hole wave functions is high for a particular level, their envelope functions have similar radial dependences. Since the hole wave function of the next level (and all other levels) is orthogonal for constant NC dimensions, the overlap will be low and that particular lobe will not give rise to high P_t. This is shown in Fig. 5, where we see that an area of high probability P_t for an exciton state is never replicated for higher states of equal symmetry; for example, the shapes of the high-P_t features in Fig. 5(b) fit in the regions in which P_t was comparatively low in Fig. 5(a).

The weakness of the $1s_{1/2}3S_{3/2}$ transition in the lower right quasi-type-II regime [Fig. 5(c)] in CdSe/CdTe can be understood in similar terms. The high-P_t region of $1s_{1/2}2S_{3/2}$ must lie in the region in which P_t is low for the lowest electron-hole pair state. Due to the proximity of the $2S_{3/2}$ and $1S_{3/2}$ levels, this region lies largely above the $2S_{3/2}$ localization boundary. For the $1s_{1/2}3S_{3/2}$ level, we see that the hole wave function has significant amplitude in the core to overlap with the electron wave function only below the $3S_{3/2}$ localization boundary [Fig. 6(c)]. However, since P_t is quite high for the $1s_{1/2}2S_{3/2}$ state over much of this region, P_t must remain low for the $1s_{1/2}3S_{3/2}$ exciton in this same area of (a,a_s) space.

B. Coulomb interaction

1. Interparticle Coulomb interaction

We found that the interparticle energy E_c tends to be suppressed in the upper left quasi-type-II regimes of the CdTe/CdSe NC and enhanced in the lower right quasi-type-II regimes of the CdSe/CdTe NC. This is caused by shifts in the distribution of hole probability density because the changes in E_c occur at the hole (but not electron) localization boundaries. We find that the effect is much smaller in CdTe/CdSe than CdSe/CdTe and that this change with localization regime originates from the direct Coulomb energy $E_{c,d}$ since $V_{c,d}$ depends on $\max(r_e,r_h)$ compared to V_p, which is essentially a piecewise constant inside the NC (Fig. 2). $E_{c,d}$ is suppressed in the upper left quasi-type-II regimes of CdTe/CdSe because the hole is delocalized over the NC which reduces the expectation value of $1/\max(r_e,r_h)$ compared to the type-II regime where the hole is core localized (with smaller mean radial coordinate). $E_{c,d}$ is enhanced in the lower right quasi-type-II regime of CdSe/CdTe because the hole is delocalized over the NC, which tends to increase the expectation value of $1/\max(r_e,r_h)$ compared to the type-II regime where it is shell localized (on average further from the center of the NC). $E_{c,d}$ follows a size dependence of approximately $1/(a + a_s)$.

2. Carrier self-energies

We focus on the hole self-energy $E_{s,h}$ since this shows the more interesting behavior of the two carriers; Fig. 7 shows the size dependence of $E_{s,h}$ for the considered hole levels. From Eq. (14), the hole self-energy is given by $E_{s,h} = \langle\Psi_h|V_s(\mathbf{r}_h)|\Psi_h\rangle$ and so reflects changes in the overlap of hole probability density with the self-polarization potential V_s. The overall (a,a_s) dependence of $E_{s,h}$ for each level arises from the interplay of contributions from the core, shell, and matrix regions, which change as the hole localizes in different regions of the NC. We label these contributions $E_{s,h,1}$, $E_{s,h,2}$, and $E_{s,h,3}$, respectively. We find that $E_{s,h,3} < 0$ for most NCs due to the attractive potential well just outside the NC surface [Fig. 2(c)], and that it is small in magnitude compared to $E_{s,h,1}$ and $E_{s,h,2}$.

For the lowest *h*/*e* NC hole level, $E_{s,h}$ is slightly enhanced to the right of the localization boundary (hole core-localized regime) compared to the left of it (delocalized regime). This is due to the fact that the increase in $E_{s,h,1}$ on crossing the boundary is nearly offset by the decrease in $E_{s,h,2}$ as the amount of probability density increases in the core and falls in the shell. Changes of the self-energy with hole localization in the *e*/*h* NC are more dramatic and can be understood in terms of the contributions $E_{s,h,1}$ and $E_{s,h,2}$. For the lowest *e*/*h* hole level, $E_{s,h}$ is dramatically enhanced with increasing a_s as the localization boundary is crossed because $E_{s,h,2}$ increases as the hole localizes in the shell—this increase is considerably larger than the corresponding decrease in $E_{s,h,1}$ due to the large peak in V_s which occurs at the NC surface [Fig. 2(c)] arising from dielectric mismatch with the surrounding matrix. The change in $E_{s,h}$ as a_s increases is greater in the (2,6)-band theory than in the single-band theory due to faster hole localization in the shell as its width increases, as shown by the more rapid decrease of p_c with a_s in Fig. 6(a). This is due to the lower hole quantization energies in the (2,6)-band model.

In general we see more dramatic changes in $E_{s,h}$ for the *e*/*h* NC because they mainly arise from changes in overlap with the large peak in V_s that occurs at the NC surface, while in the *h*/*e* NC they arise from changes in the overlap with V_s in the core region where it is approximately constant [see Fig. 2(c)]. We find a complicated size dependence of the self-energy for the higher levels, which can be understood by considering Fig. 6 and the relative contributions of $E_{s,h,1}$ and $E_{s,h,2}$. For example, for the *e*/*h* single-band $2S$ level $E_{s,h}$ is suppressed below the hole localization boundary relative to above it, exhibiting a minimum shown by the bending of the constant-energy contours [Fig. 7(b)]. We see for the corresponding (2,6)-band level that, although the self-energy is suppressed for shell widths less than ≈1.2 nm, there is a local maximum below the hole localization boundary. Comparing Figs. 6 and 7, we can see that areas of (a,a_s) space where p_c is high are associated with areas in with suppressed hole self-energy in the CdSe/CdTe NC because these NC designs are localizing the hole away from the large peak in V_s at the NC surface. We also find that local maxima in $E_{s,h}$ as a function of a_s correspond to local minima in the probability p_c that occur between the high probability lobes in Fig. 6. This is seen for the $2S_{3/2}$ and $3S_{3/2}$ levels of CdSe/CdTe NCs with thin shells ($a_s \approx 0.5$ nm).

We find that the size dependence of the hole self-energy for the $2S$ and $3S_{3/2}$ levels is quite similar in the two models, due to their similar energies and hole localization. The latter

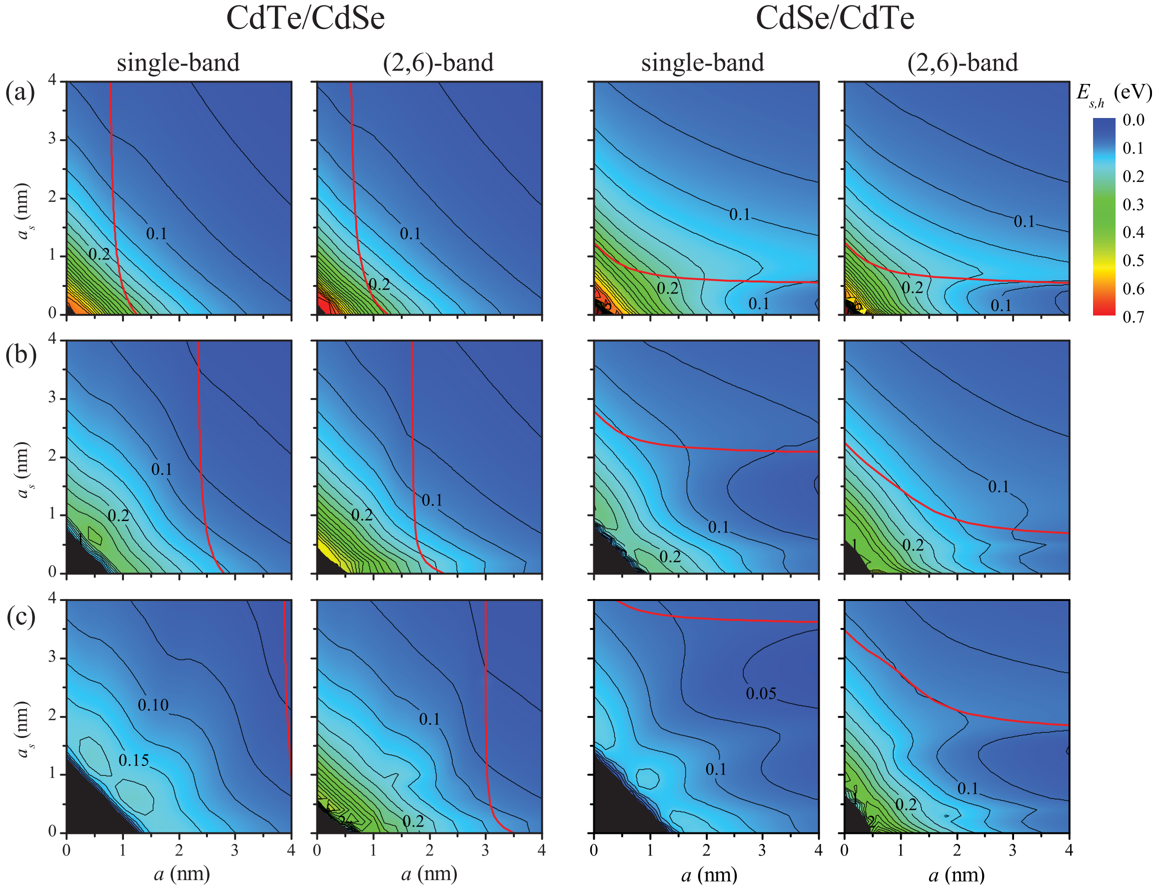

FIG. 7. (Color online) Hole self-energy $E_{s,h}$ for CdTe/CdSe and CdSe/CdTe NCs calculated in the single-band model (first and third columns) and the (2,6)-band model (second and fourth columns) for the nS and $nS_{3/2}$ levels; rows (a), (b), and (c) correspond to $n = 1$, 2, and 3. Red lines represent hole localization boundaries and constant-energy contours (black lines) are spaced at 25 meV intervals with labels in eV.

is reflected in the similarity of the plots of the probability p_c for the $2S$ and $3S_{3/2}$ levels (Fig. 6).

3. Absorption wavelengths

Figure 8 shows the predicted absorption wavelengths for the $1s_{1/2}nS_{3/2}$ and $1snS$ ($n = 1,2,3$) excitons in the CdTe/CdSe and CdSe/CdTe NCs calculated with $\varepsilon_{\text{out}} = 2$ and $\delta_1 = \delta_2 = 0.1$ nm. We show wavelengths as constant-energy contours to facilitate comparison with experimental data. Electron and hole localization boundaries are shown as dashed black and red lines, respectively. As expected, the shortest wavelengths occur in the type-I regimes (which correspond to the smallest NCs) and the longest in the type-II regimes (the largest NCs). We see that the type-II band alignments of both NCs allow for absorption wavelengths that span most of the visible spectrum, from ~450 nm in the type-I regime to ~860 nm in the type-II regime for the lowest optically active exciton; this can be compared with the bulk absorption wavelengths of 709 nm for CdSe and 795 nm for CdTe predicted using the parameters in Table I. Overall, we see that the single-band model predicts similar wavelengths to the more sophisticated theory for the ground state exciton of both structures but significantly different wavelengths for higher excitons. Most of the discrepancy for the latter comes from the difference between the predicted hole quantization energies, due to the divergence of the single-band hole dispersion from the $J = 3/2$ valence bands. We see that wavelengths predicted for the $2S$ and $3S_{3/2}$ levels are similar, showing that the single-band model in effect "misses" a level predicted by the (2,6)-band theory when using the parameters listed in Table I.

We find that inclusion of the Coulomb interaction is necessary for quantitative agreement with experimental data, particularly for the CdSe/CdTe NC where the change in hole self-energy with localization regime significantly affects the absorption wavelengths. The suppression of $E_{s,h}$ when the hole is delocalized over the NC leads to considerable redshift of the absorption wavelengths in the lower right quasi-type-II regimes reflected by the distortion of the constant wavelength contours in those regions (see Fig. 8). This effect is seen in both models, but is more marked in the (2,6)-band theory due to stronger hole localization in the shell region as its width increases. Such changes in absorption should be easily measurable by experiment and could provide a useful test of the model used for the Coulomb interaction in these structures.

In Fig. 9 we compare our model results for CdTe/CdSe NCs with the absorption spectra measured by Oron *et al.*[37] for NCs with a 1.95 nm radius core and different shell thicknesses.

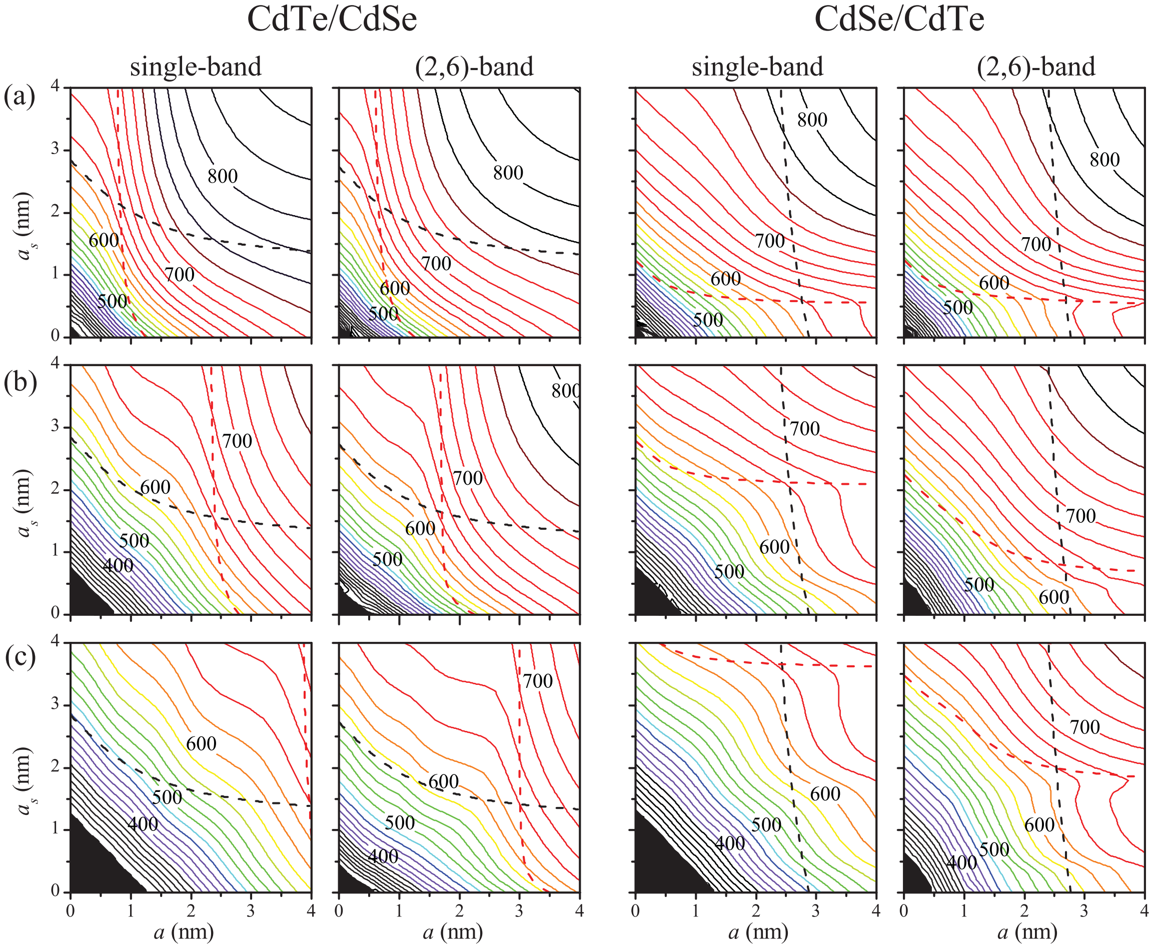

FIG. 8. (Color online) Exciton absorption wavelengths for CdTe/CdSe and CdSe/CdTe NCs calculated in the single-band and (2,6)-band models. The single-band wavelengths of the $1snS$ excitons are shown in the first and third columns, the (2,6)-band wavelengths of the $1s_{1/2}nS_{3/2}$ excitons in the second and fourth columns; rows (a), (b), and (c) correspond to $n = 1$, 2, and 3. Constant-wavelength contours are separated by 20 nm intervals and labels are in units of nanometers. Electron and hole localization boundaries are shown as dashed black and red lines, respectively.

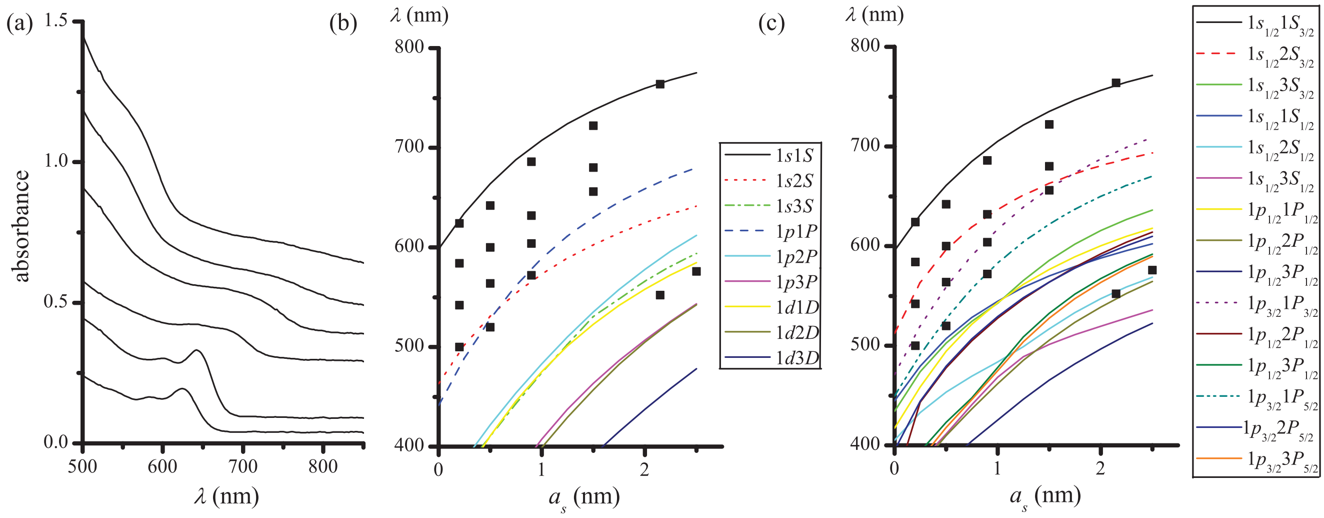

FIG. 9. (Color online) (a) Absorption spectra[37] of CdTe/CdSe core-shell NCs having $a = 1.95$ nm cores and shells of thickness 0.2, 0.5, 0.9, 1.5, 2.15, and 2.5 nm. Spectra are vertically offset for clarity. (b) Calculated absorption wavelengths in the single-band theory. Absorption features extracted from the spectra in (a) are shown as black squares. (c) Absorption wavelengths calculated in the (2,6)-band theory. Legends to the right of (b) and (c) indicate the exciton transition corresponding to each wavelength line.

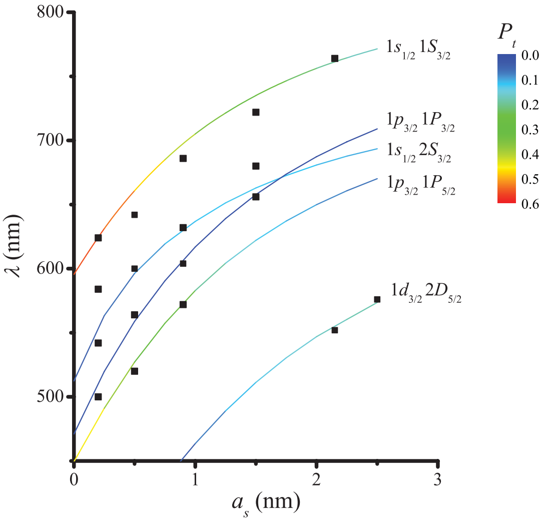

FIG. 10. (Color online) Absorption wavelengths of the exciton transitions identified using the (2,6)-band theory. Lines are color coded to show the associated excitation probability, and the five exciton states we assign to features in the absorption spectra are labeled on the right. Absorption features identified in the data of Oron *et al.*[37] are shown as black squares.

For the single-band theory [Fig. 9(b)] we show all allowed transitions involving electron states up to $l = 2$, and for the (2,6)-band theory [Fig. 9(c)] we show all dipole-allowed transitions involving electron states up to $1p_{3/2}$. We note that only the $l = 0$ component of V_c [Eq. (12)] is needed to calculate E_c if the electron is in a spherically symmetric state. Higher angular momentum electron states invoke higher terms in l of V_c (see Ref. 31 for full definition). Due to the forms of the wave functions this leads to larger corrections in E_c in the single-band theory than the (2,6)-band theory and shifts of up to ~15 nm in the calculated wavelengths of the single-band theory compared to < 5 nm for the (2,6)-band theory.

Absorption peak positions were extracted from data provided by Oron *et al.* using the Savisky-Golay smoothed second derivative of the data and are shown as black squares [Figs. 9(b) and 9(c)]. We see that both models predict the size dependence of the ground state exciton energy quite well. However, the single-band theory completely fails to predict the correct positions of the second and third absorption features due to the artificially high hole quantization energies produced by the parabolic valence band dispersion. Single-band theory also underestimates the number of transitions compared to the (2,6)-band theory since only transitions which have $\Delta l = 0$ are allowed due to the orthogonality of the spherical harmonics (see Sec. II A 1). In contrast, *s*-*d* mixing in the (2,6)-band theory means that each hole wave function $\Psi^h_{j,m}$ is essentially a superposition of envelope functions with orbital angular momenta $j - \frac{1}{2}$ and $j + \frac{3}{2}$ [see Eq. (5)] giving rise to more allowed transitions.

The (2,6)-band theory predicts the energies of second and third absorption features reasonably well, although it tends to diverge from the data for thin shells ($a_s \approx 0.2$ nm). This may be due to failure of the effective mass theory as the shell thickness approaches 1 monolayer. The energy of the third transition is accurately predicted by the theory for $a_s > 0.5$ nm. Although the difference between experiment and theory is greater for the second transition, we see that the data show a decreasing energy gap with increasing shell thickness. This suggests that the crossing of the second and third exciton levels does occur, but at a larger shell thickness than predicted by the theory.

Despite differences with the data, the (2,6)-band theory allows us to unambiguously identify the second, third, and fourth absorption features as due to the $1s_{1/2}2S_{3/2}$, $1p_{3/2}1P_{3/2}$, and $1p_{3/2}1P_{5/2}$ excitons. It also allows us to tentatively identify the broad, strengthening absorption feature seen around 575 nm for the last two NCs in the size series [Fig. 9(a)] as due to the $1d_{3/2}2D_{5/2}$ exciton. We make this assignment on the basis of its energy and increasing excitation probability P_t with shell thickness compared to nearby transitions: Fig. 10 shows the absorption wavelengths of the five exciton states we identify using the (2,6)-band theory, with lines color coded to show the excitation probability. We see that the ground state exciton has the highest excitation probability (as expected), but higher transitions can have comparable values if the radial character of the electron and hole wave functions is similar.

IV. CONCLUSIONS

Spherical type-II NCs were modeled using a single-band and a (2,6)-band EMA, including the effects of a finite confining potential. We calculated single-particle states as a function of core radius and shell thickness and identified localization regimes. We found close agreement between the two EMA models for the carrier ground states, but divergence of the hole energies for $n > 1$ due to the difference between the parabolic hole dispersion and the lh and hh valence bands in CdSe. We found that for CdSe/CdTe NCs the single-band model effectively misses the hole level which should energetically correspond to $2S_{3/2}$ in the (2,6)-band theory. We showed that hole wave function orthogonality affects the (a,a_s) dependence of the hole localization of successive levels, which in turn affects the size dependence of the excitation probabilities. We also found that excitation probabilities are potentially smaller in the (2,6)-band model due to the mixed *s*-*d* symmetry of the hole wave functions and the fact that only the $J = 3/2$ valence bands contribute to the oscillator strength. In contrast, hole states in the single-band model are pure *S* states which can in theory have perfect overlap with the electron wave function. The absence of *s*-*d* mixing in the single-band theory also means it significantly underestimates the number of allowed transitions. We included the Coulomb interaction as a first-order perturbation, including interparticle and polarization charge effects. We calculated absorption wavelengths as a function of core radius and shell thickness for three exciton states in each theory. We found that both models predict a suppression of the hole self-energy in the quasi-type-II regime of the CdSe/CdTe ground state exciton which should have a measurable effect on transition wavelengths. We compared calculated absorption wavelengths with experimental data for CdTe/CdSe NCs and found that for $\delta_1 = \delta_2 = 0.1$ nm, $\varepsilon_3 = 2$, and $E_{v1} = 0.4$ eV both models predict the size dependence of the exciton ground state quite accurately, but the single-band theory completely fails to predict the energies of the second and third absorption features correctly. The (2,6)-band theory allowed us to identify the second, third, and fourth exciton states as $1s_{1/2}2S_{3/2}$, $1p_{3/2}1P_{3/2}$, and $1p_{3/2}1P_{5/2}$. We tentatively assigned the broad absorption feature around 575 nm to the $1d_{3/2}2D_{5/2}$ exciton for the last two NCs in the size series measured by Oron *et al.*[37]

ACKNOWLEDGMENTS

This work was funded by the UK Engineering and Physical Sciences Research Council. The authors would like to thank V. A. Fonoberov for helpful communications and D. Oron for nanocrystal absorption data.

---

[1] M. A. Hines and P. Guyot-Sionnest, J. Phys. Chem. **100**, 468 (1996).

[2] B. O. Dabbousi, J. Rodriguez-Viejo, F. V. Mikulec, J. R. Heine, H. Mattoussi, R. Ober, K. F. Jensen, and M. G. Bawendi, J. Phys. Chem. B **101**, 9463 (1997).

[3] A. Mews, A. V. Kadavanich, U. Banin, and A. P. Alivisatos, Phys. Rev. B **53**, R13242 (1996).

[4] A. Mews, A. Eychmuller, M. Giersig, D. Schooss, and H. Weller, J. Phys. Chem. **98**, 934 (1994).

[5] F. Shieh, A. E. Saunders, and B. A. Korgel, J. Phys. Chem. B **109**, 8538 (2005).

[6] D. J. Milliron, S. M. Hughes, Y. Cui, L. Manna, J. Li, L.-W. Wang, and A. P. Alivisatos, Nature (London) **430**, 190 (2004).

[7] A. Piryatinski, S. A. Ivanov, S. Tretiak, and V. I. Klimov, Nano Lett. **7**, 108 (2007).

[8] B. Kraabel, A. Malko, and V. I. Klimov, Appl. Phys. Lett. **78**, 1814 (2001).

[9] M. A. Petruska, A. Malko, P. M. Voyles, and V. I. Klimov, Adv. Mater. **15**, 610 (2003).

[10] S. A. Ivanov, J. Nanda, A. Piryatinski, M. Achermann, L. P. Balet, I. V. Bezel, P. O. Anikeeva, S. Tretiak, and V. I. Klimov, J. Phys. Chem. B **108**, 10625 (2004).

[11] R. D. Schaller and V. I. Klimov, Phys. Rev. Lett. **92**, 186601 (2004).

[12] R. D. Schaller, V. M. Agranovich, and V. I. Klimov, Nature Phys. **1**, 189 (2005).

[13] J. Nanda, S. A. Ivanov, H. Htoon, I. Bezel, A. Piryatinski, S. Tretiak, and V. I. Klimov, J. Appl. Phys. **99**, 034309 (2006).

[14] J. Nanda, S. A. Ivanov, M. Achermann, I. Bezel, A. Piryatinski, and V. I. Klimov, J. Phys. Chem. C **111**, 15382 (2007).

[15] S. A. Ivanov, A. Piryatinski, J. Nanda, S. Tretiak, K. R. Zavadil, W. O. Wallace, D. Werder, and V. I. Klimov, J. Am. Chem. Soc. **129**, 11708 (2007).

[16] E. P. Pokatilov, V. A. Fonoberov, V. M. Fomin, and J. T. Devreese, Phys. Rev. B **64**, 245328 (2001).

[17] E. P. Pokatilov, V. A. Fonoberov, V. M. Fomin, and J. T. Devreese, Physica E **26**, 63 (2005).

[18] P. C. Sercel and K. J. Vahala, Phys. Rev. B **42**, 3690 (1990).

[19] T. Richard, P. Lefebvre, H. Mathieu, and J. Allègre, Phys. Rev. B **53**, 7287 (1996).

[20] P. C. Sercel, Al. L. Efros, and M. Rosen, Phys. Rev. Lett. **83**, 2394 (1999).

[21] D. Schooss, A. Mews, A. Eychmuller, and H. Weller, Phys. Rev. B **49**, 17072 (1994).

[22] D. J. BenDaniel and C. B Duke, Phys. Rev. **152**, 683 (1966).

[23] L. E. Brus, J. Chem. Phys. **79**, 5566 (1983).

[24] M. G. Burt, J. Phys.: Condens. Matter **4**, 6651 (1992).

[25] M. G. Burt, Phys. Rev. B **50**, 7518 (1994).

[26] M. G. Burt, J. Phys.: Condens. Matter **11**, R53 (1999).

[27] A. L. Efros and M. Rosen, Phys. Rev. B **58**, 7120 (1998).

[28] V. A. Fonoberov, E. P. Pokatilov, and A. A. Balandin, J. Nanosci. Nanotechnol. **3**, 253 (2003).

[29] A. L. Efros, Phys. Rev. B **46**, 7448 (1992).

[30] V. A. Fonoberov and A. A. Balandin, J. Appl. Phys. **94**, 7178 (2003).

[31] P. G. Bolcatto and C. R. Proetto, J. Phys.: Condens. Matter **13**, 319 (2001).

[32] Only the $l = 0$ component of V_c (see Ref. 31) is needed to calculate E_c if the electron state is spherically symmetric. Higher angular momentum states invoke higher l terms of V_c; see Section III B 3.

[33] J. M. Rowe, R. M. Nicklow, D. L. Price, and K. Zanio, Phys. Rev. B **10**, 671 (1974).

[34] L. W. Wang and A. Zunger, Phys. Rev. B **53**, 9579 (1996).

[35] H.-S. Sheu, U.-S. Jeng, W.-J. Shih, Y.-H. Lai, C.-H. Su, C.-W. Lai, M.-J. Yang, Y.-C. Chen, and P.-T. Chou, J. Phys. Chem. C **112**, 9617 (2008).

[36] S. Schulz and G. Czycholl, Phys. Rev. B **72**, 165317 (2005).

[37] D. Oron, M. Kazes, and U. Banin, Phys. Rev. B **75**, 035330 (2007).

[38] E. P. Pokatilov, V. A. Fonoberov, V. M. Fomin, and J. T. Devreese, Phys. Rev. B **64**, 245329 (2001).

[39] C. de Mello Donega and R. Koole, J. Phys. Chem. C **113**, 6511 (2009).

[40] D. J. Norris and M. G. Bawendi, Phys. Rev. B **53**, 16338 (1996).

[41] Y. Masumoto and K. Sonobe, Phys. Rev. B **56**, 9734 (1997).

[42] M. C. Beard, G. M. Turner, and C. A. Schmuttenmaer, Nano. Lett. **2**, 983 (2002).

[43] X-ray diffraction measurements on the CdTe cores used to grow CdTe/CdSe NCs by Oron *et al.* (Ref. 36) showed a zinc-blende structure (private communication).

[44] The energy dependence of the hole radial Hamiltonian means that radial wave functions deviate from orthonormality by $\sim 1\%$.